Photothermal-wave diffraction and interference in condensed media: experimental evidence in aluminum

Andreas Mandelis and Kwan F. Leung

Photoacoustic and Photothermal Sciences Laboratory, Ontario Laser and Lightwave Research Center, Department of Mechanical Engineering, University of Toronto, Toronto, Ontario M5S 1A4, Canada

Received October 23, 1989; accepted April 3, 1990

Thermal-wave fields have been optically generated and measured, using spatially resolved scanning photopyroelectric detection. Both single laser-beam diffraction profiles and thermal-wave patterns from two laser beams, interfering coherently in a manner analogous to Young's optical-wave experiment, have been produced. The diffraction and interference images have further been shown to be in excellent qualitative agreement with a Laplace thermal-wave propagation formalism, which treats thermal-wave diffraction in the small-aperture approximation. A mechanism for quantitative agreement was obtained after the finite size of the probing metal detector tip was taken into account in mapping thermal-wave fields.

1. INTRODUCTION

The peculiar nature of thermal waves as spatially heavily damped pseudowaves[1] is mathematically the result of a specific, Helmholtz wavelike form of the Fourier heat conduction equation. This equation holds instead of a proper Helmholtz wave equation and predicts the propagation of exponentially damped plane thermal waves in the bulk of a condensed phase medium. In a general three-dimensional (3-D) theoretical framework, such pseudowaves have been shown[2] to possess diffractive and interference characteristics. A diffraction integral has been established in the experimentally justifiable limit of a small-aperture (SA) approximation, which permits analytical treatments of thermal-wave fields generated by arbitrary aperture functions. The field functions can thus be obtained as spatial convolutions of the aperture function with the thermal-wave spatial impulse response by using Laplace thermal-wave physics (in analogy to Fourier optics). It is important to note that the reason that a spatial Laplace transform formalism, rather than a Fourier transform approach, is appropriate to thermal-wave field propagation and diffraction is that the thermal-wave vector (and wave number) is complex, rotated 45 deg with respect to proper (real) wave vectors in the complex plane. This results in a diffraction integral in the SA approximation, which can be readily identified as a two-dimensional spatial Laplace transform.[2]

Recently a three-dimensional, spatial Fourier-transform-based formalism of the heat conduction equation has been used to obtain solutions for propagating thermal-wave fields in thermally isotropic[3] and anisotropic[4] solid media, generated by circularly symmetric optical sources, such as Gaussian laser beams. That type of treatment results in a straightforward solution for the thermal-wave fields induced by the (assumed) circularly symmetric photothermal aperture, through numerical integration of the Hankel transform of the field across a cross-sectional plane perpendicular to the direction of propagation. It does not, however, comprise a proper diffraction integral, which corresponds to the particular pseudowave form of the Helmholtz-like thermal-wave equation[2] and can conveniently give explicit analytical expressions for the thermal-wave field functions generated by arbitrary aperture functions. This important feature, which eliminates the requirement for circularly symmetric apertures, is vital to the description of composite fields generated through spatially interfering sources[2] from which circular symmetry cannot be obtained. Nevertheless, the Fourier–Bessel transformation-based approach has been successful in yielding reasonable theoretical predictions for narrow Gaussian source apertures corresponding to tightly focused laser beams.

In this paper the theoretical prediction[2] for the diffraction field generated from a photothermal aperture function, as well as the predictions[2] for the interference fields resulting from two photothermal apertures operating coherently (in phase) or anticoherently (out of phase), has been tested experimentally. The effects of the finite size of the thermal-wave probe tip have also been treated theoretically, and the resulting broadening of the field function has been shown to be in good agreement with experimental spatial profiles of the thermal-wave field. This treatment thus accounts for observed quantitative discrepancies between theory and experiment and identifies the probe tip size as an important practical factor limiting resolution in imaging applications.

2. THEORETICAL BACKGROUND AND NUMERICAL SIMULATIONS

Diffraction

The geometry of laser-beam-generated thermal-wave propagation in 3-D space is shown in Fig. 1. Under the condition of the SA approximation, a convenient representation of the diffraction integral can be written that encompasses all field locations on the observation plane, such that $r_0 > \rho$ in Fig. 1, where $(r_0, \Psi_0) \leftrightarrow (x, y)$ are observation plane variables and $(\rho, \Psi_1) \leftrightarrow (\zeta, \eta)$ are aperture plane variables. Experimentally, when focused laser beams are used, the SA approximation

0740-3232/91/010186-15$05.00

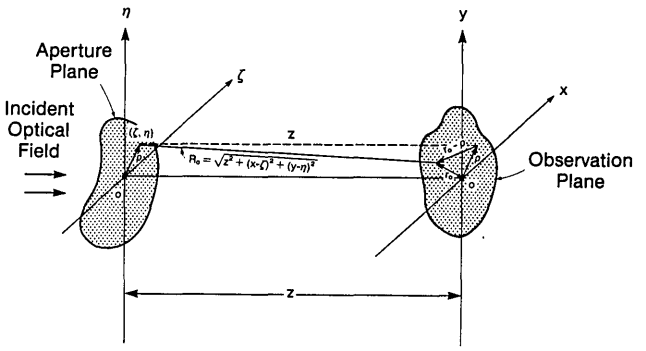

Fig. 1. Photothermal-wave diffraction geometry.

is valid for essentially all field positions outside the symmetry axis of the exciting laser beam.[2] The diffraction integral then becomes

$$T(r_0, z) = \frac{\exp(i\pi/4)}{4i\lambda_t}\left(\frac{z}{R}\right)\frac{\exp[-(1-i)k_s R]}{R}K(r_0, z), \quad (1)$$

where

$$K(r_0, z) \equiv {}^2L_B\{T_0(\rho)\exp[-(s/2r_0)\rho^2]\}|_{\rho=s}. \quad (2)$$

In Eqs. (1) and (2) a circularly symmetric aperture function has been assumed. $T(r_0, z)$ is the temperature field at field location

$$R = (x^2 + y^2 + z^2)^{1/2} = (r_0{}^2 + z^2)^{1/2}. \quad (3)$$

$T_0(\rho)$ is the optically generated photothermal source function on the aperture plane, assuming a high optical absorption coefficient and thus surface absorption only (e.g., visible radiation incident upon a blackened metal surface–aperture plane). In Eq. (1) λ_t is the thermal wavelength at angular modulation frequency ω:

$$\lambda_t(\omega) = 2\pi(\alpha/\omega)^{1/2}, \quad (4a)$$

with α the sample thermal diffusivity. k_s is the thermal diffusion coefficient:

$$k_s(\omega) = (\omega/2\alpha)^{1/2}. \quad (4b)$$

In Eq. (2) $K(r_0, z)$ stands for the two-dimensional spatial Laplace–Bessel transform of the function within the braces,[2] to be evaluated at $\rho = s \equiv 2\pi \exp(-i\pi/4)f_{r_0}$, where f_{r_0} is a polar thermal-wave spatial frequency:

$$f_{r_0} \equiv r_0/\lambda_t R. \quad (5)$$

For the TEM_{00} mode of a Gaussian laser beam, the aperture profile of unit magnitude is given by

$$T_0(\rho) = \exp(-\rho^2/w^2), \quad (6)$$

where w is the beam waist. Equations (1) and (2) then yield the complex diffraction photothermal-wave temperature field, which can be written in terms of its experimentally relevant components, amplitude and phase, as follows[2]:

$$|T(r_0, z)| = \frac{1}{16\sqrt{2}}\left[\frac{k_s z}{R^2(F_1{}^2 + F_2{}^2)^{1/2}}\right] \times \exp\left\{-\left[k_s R + \frac{(k_s/R)^2 F_2}{2(F_1{}^2 + F_2{}^2)}r_0{}^2\right]\right\} \quad (7)$$

and

$$\phi(r_0, z) = -\frac{\pi}{4} + k_s R + \frac{(k_s r_0/R)^2 F_1}{2(F_1{}^2 + F_2{}^2)} + \tan^{-1}(F_2/F_1), \quad (8)$$

where

$$F_1(R, w) \equiv \frac{1}{w^2} + \frac{k_s(\omega)}{2R} \quad (9)$$

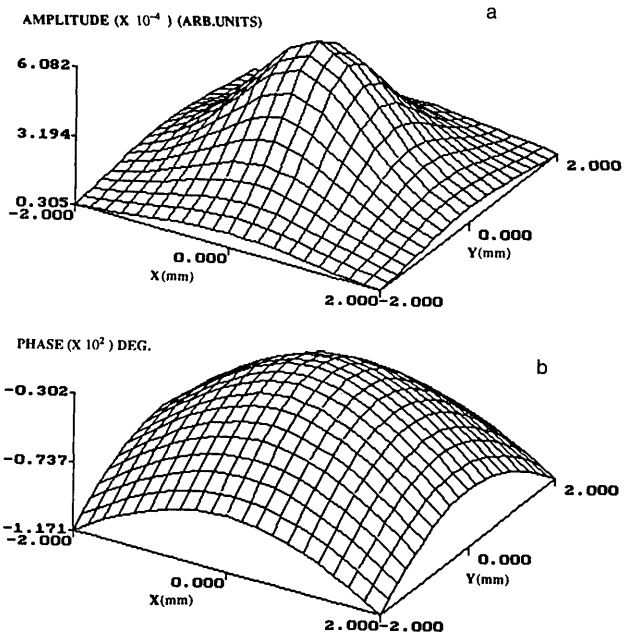

Fig. 2. Theoretical simulation of thermal-wave diffraction field generated by a $w = 300$-μm laser beam impinging upon the surface ($z = 0$) of a semi-infinite aluminum sample ($\alpha_{Al} = 0.82$ cm^2/sec). The temperature field is shown at $z = 1.5$ mm. Modulation frequency 20 Hz: a, amplitude; b, phase.

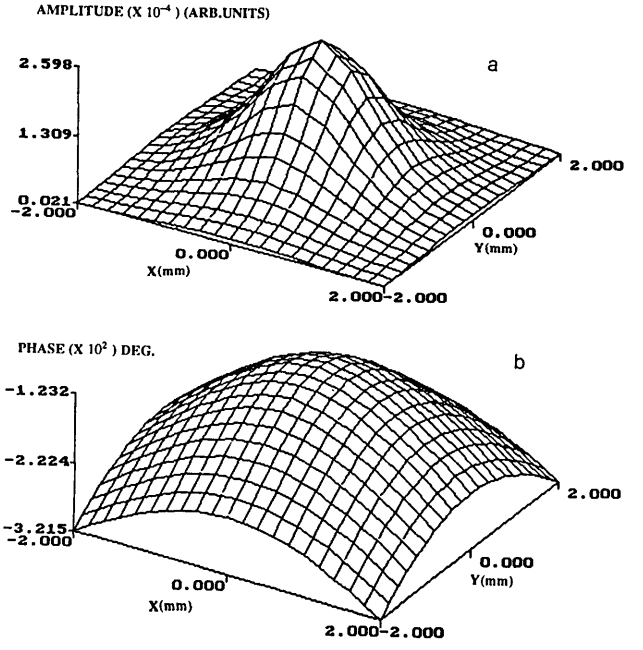

Fig. 3. Same as in Fig. 2 but for modulation frequency 100 Hz.

and

$$F_2(R) \equiv \frac{k_s(\omega)}{2R}. \tag{10}$$

Figures 2 and 3 show numerical results obtained using Eqs. (7) and (8) with an assumed exciting Gaussian laser beam of $w = 300$ μm located at the origin ($\zeta = \eta = 0$). The simulations of Figs. 2 and 3 assume an aluminum medium with thermal diffusivity[5] of 0.82 cm^2/sec and laser-beam irradiance modulation frequencies of 20 and 100 Hz, respectively. These frequencies were chosen to satisfy the thermally thick limit[6]

$$k_s(\omega)R \gg 1 \tag{11}$$

on the observation plane $z = 1.5$ mm. This consideration is important, for it is in this limit that Eq. (1) is strictly valid.[2] The thermally thin case[6] may also be easily handled after Eq. (2) is slightly modified by multiplying the expression $T_0(\rho)$ within the braces by the factor[2]

$$1 + \frac{\exp(i\pi/4)}{\sqrt{2}k_s(\omega)R}\left[1 + \left(\frac{r_0}{R^2}\right)\rho\right]. \tag{12}$$

A comparison of Figs. 2 and 3 shows a steeper decay of the diffraction amplitude in the radial direction at 100 Hz, an expected feature leading to the enhancement of spatial resolution.[7,8] The resolution increase, however, is accompanied by a decrease in the absolute magnitude of the field function, in agreement with previous reports.[3,6] The phase profiles are broader than the respective amplitudes and indicate increasing lags with increasing radial distance from the source, as expected.[7] The net phase lag at a given coordinate point is always greater in the 100-Hz case (Fig. 3b) and is also in agreement with the photothermal origin of the field function.[9]

Figure 4 indicates that the effect of the exciting laser-beam waist size is quite small in the 30- to 800-μm range. This result, in turn, indicates that the resolution of the diffraction field is only weakly dependent on the laser-beam size in the above range and is a guide to the design of the optical part of the experimental setup.

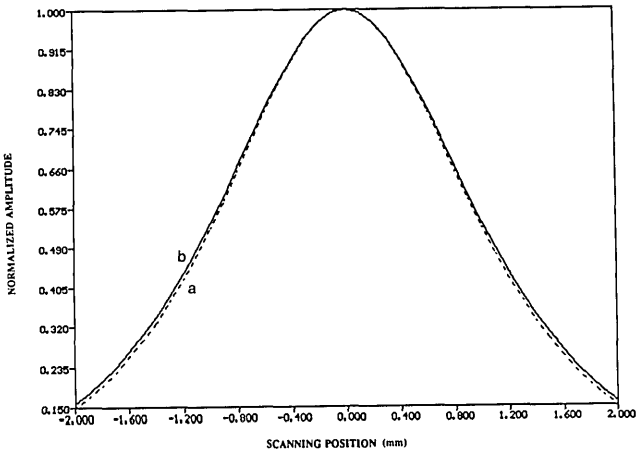

Fig. 4. Theoretical simulation of the normalized thermal-wave diffraction field of Fig. 2 generated with laser-beam spot sizes a, $w = 30$ μm and b, $w = 800$ μm.

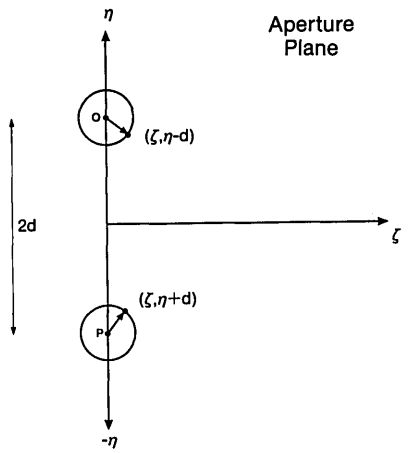

Fig. 5. Photothermal-wave interference geometry on the aperture plane (ζ, η).

Interference

The geometry of thermal-wave interference fields generated by two laser beams incident upon a material surface, a distance $2d$ from each other along the η axis of the aperture plane, is shown in Fig. 5. Because circular symmetry is broken when two photothermal sources are considered, a Cartesian coordinate representation (x, y, z) of the superposition thermal-wave field becomes necessary,[2] thus forcing one to abandon the simpler polar coordinate formulation (r_0, z). Under these conditions the diffraction integral, Eq. (1), may be written in Cartesian coordinates[2]:

$$T(x, y, z) = \frac{\exp(i\pi/4)}{4i\lambda_t}\left(\frac{z}{R}\right)\frac{\exp[-(1-i)k_sR]}{R}Q(x, y, z), \tag{13}$$

where

$$Q(x, y, z) \equiv {}^2L\{T_0(\zeta, \eta)\exp[-(s_x\zeta^2/2x)]\exp[-(s_y\eta^2/2y)]\}. \tag{14}$$

In Eqs. (13) and (14) $Q(x, y, z)$ is the two-dimensional spatial Laplace transform of $T_0(\zeta, \eta)$ to be evaluated at $s_x = 2\pi \exp(-i\pi/4)f_x$ and $s_y = 2\pi \exp(-i\pi/4)f_y$, where f_x and f_y are Cartesian spatial frequencies:

$$f_x \equiv \frac{x}{\lambda_t R}, \qquad f_y \equiv \frac{y}{\lambda_t R}. \tag{15}$$

Assuming that two exciting laser beams of unit irradiance have Gaussian TEM_{00} profiles of equal spatial spot sizes ($w_1 = w_2 \equiv w$), and also assuming in-phase operation (constructive interference indicated by the +) or out-of-phase operation (destructive interference indicated by the −), we obtain source functions (see Fig. 5):

$$T_0^{\pm}(\zeta, \eta) = \exp\{-[\zeta^2 + (\eta - d)^2]/w^2\} \pm \exp\{-[\zeta^2 + (\eta + d)^2]/w^2\}. \tag{16}$$

Now insertion of Eq. (16) into Eq. (14) yields complex expressions[2] for the temperature field in either case of photothermal-wave interference. These expressions can also be reduced to convenient amplitude and phase components as follows[2]:

$$|T^{(\pm)}(x, y, z)| = \frac{k_s z |N_1||N_2^{(\pm)}|}{16\sqrt{2}R^2(F_1^2 + F_2^2)^{1/2}} \exp[-(k_s R + d^2/w^2)] \tag{17}$$

and

$$|N_1| \equiv \{[\text{Re } W(z_1)]^2 + [\text{Im } W(z_1)]^2\}^{1/2}, \tag{18}$$

with

$$|N_2^{(\pm)}| \equiv \{[\text{Re } W(z_2) \pm \text{Re } W(z_3)]^2 + [\text{Im } W(z_2) \pm \text{Im } W(z_3)]^2\}^{1/2}. \tag{19}$$

In Eqs. (18) and (19) the complex function definitions were made:

$$W(z) \equiv \exp(z^2)\text{erfc}(z), \tag{20}$$

$$z_j \equiv |z_j|\exp(i\theta_j), \qquad j = 1, 2, 3, \tag{21}$$

with

$$|z_1| = \frac{k_s|x|}{\sqrt{2}R(F_1^2 + F_2^2)^{1/4}}, \qquad \theta_1 = \frac{1}{2}\tan^{-1}(F_2/F_1) - \frac{\pi}{4}; \tag{22}$$

also

$$|z_2| = \frac{(F_3^2 + F_4^2)^{1/2}}{2(F_1^2 + F_2^2)^{1/4}}, \tag{23}$$

$$\theta_2 = \tfrac{1}{2}\tan^{-1}(F_2/F_1) - \tan^{-1}(F_4/F_3), \tag{24}$$

where we have defined

$$F_3(x, y, z; d) \equiv \frac{k_s y}{R} - \frac{2d}{w^2}, \tag{25}$$

$$F_4(x, y, z) = \frac{k_s y}{R}. \tag{26}$$

Finally,

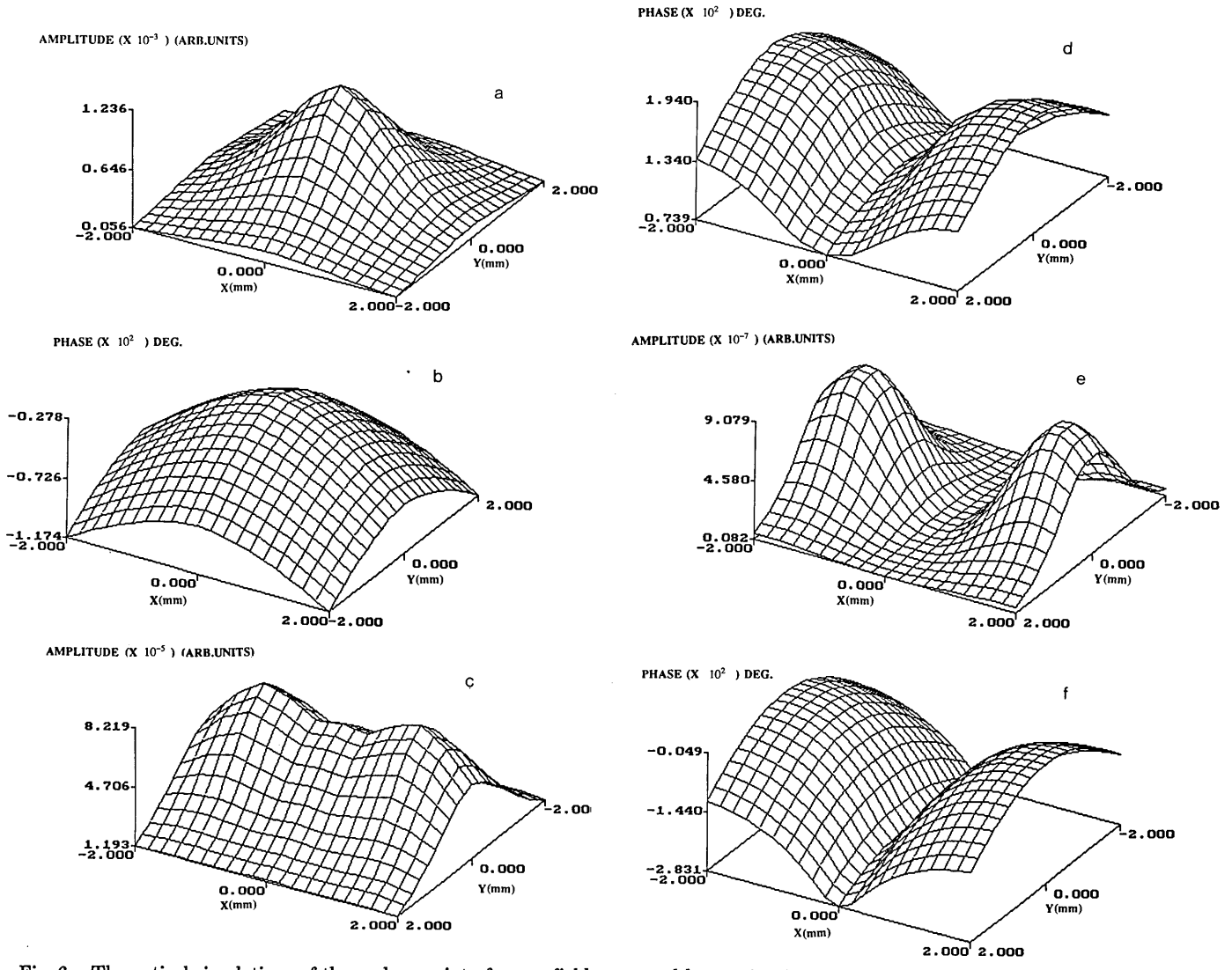

Fig. 6. Theoretical simulations of thermal-wave interference field generated by two in-phase modulated laser beams of equal irradiances impinging upon the surface ($z = 0$) of a semi-infinite aluminum sample. Beam waists are 300 μm each, and the temperature field is shown at z = 1.5 mm: a, $2d$ = 0.0 mm, f = 18 Hz, amplitude; b, phase of a; c, $2d$ = 1.8 mm, f = 18 Hz, amplitude; d, phase of c; e, $2d$ = 1.8 mm, f = 100 Hz, amplitude; f, phase of e.

$$|z_3| = \frac{(F_5^2 + F_4^2)^{1/2}}{2(F_1^2 + F_2^2)^{1/4}}, \tag{27}$$

$$\theta_3 = \tfrac{1}{2}\tan^{-1}(F_2/F_1) - \tan^{-1}(F_4/F_5), \tag{28}$$

where

$$F_5(x, y, z; d) \equiv \frac{k_s y}{R} + \frac{2d}{w^2}. \tag{29}$$

The phase of the interference thermal-wave field can then be written as

$$\Psi^{(\pm)}(x, y, z) = -\frac{\pi}{4} + k_s R + \tan^{-1}(F_2/F_1) + \phi_1 + \phi_2^{(\pm)}, \tag{30}$$

where

$$\phi_1 \equiv \tan^{-1}\left[\frac{\text{Im } W(z_1)}{\text{Re } W(z_1)}\right] \tag{31}$$

and

$$\phi_2^{(\pm)} \equiv \tan^{-1}\left[\frac{\text{Im } W(z_2) \pm \text{Im } W(z_3)}{\text{Re } W(z_2) \pm \text{Re } W(z_3)}\right]. \tag{32}$$

For computational purposes, series expressions for Re $W(z_j)$ and Im $W(z_j)$ can be found readily in Appendix A.

Figure 6 shows a series of simulations of the constructive interference field generated by a two-laser geometry as in Fig. 5. The spatial structure of thermal-wave field amplitudes and of the associated phases is depicted at a depth of 1.5 mm from the surface. In Figs. 6a and 6b the two optical beams are exactly superposed on each other ($d = 0$ in Fig. 5). Both beams are modulated in phase at $f = 18$ Hz. As a result the interference pattern shown is very similar to the single-beam diffraction pattern of Fig. 2 in both amplitude and phase channels. The maximum amplitude of the interference pattern (Fig. 6a) is, in fact, twice as large as that of the diffraction pattern from a single laser source at 18 Hz, as expected from the additive nature of the components in $|N_2^{(+)}|$ for $d = 0$ [Eq. (19)] and physically from the indistinguishability between two superimposed unit-irradiance la-

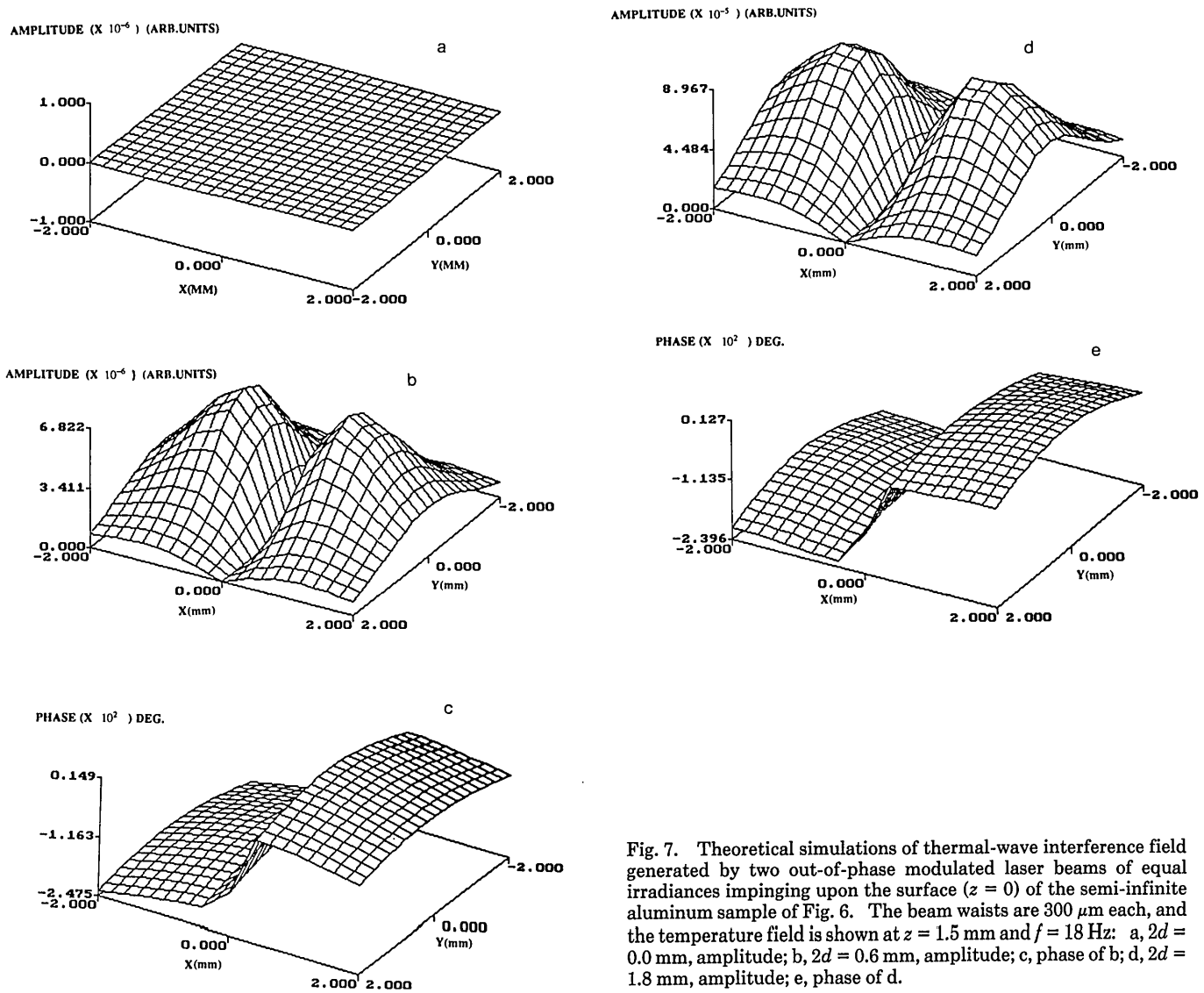

Fig. 7. Theoretical simulations of thermal-wave interference field generated by two out-of-phase modulated laser beams of equal irradiances impinging upon the surface ($z = 0$) of the semi-infinite aluminum sample of Fig. 6. The beam waists are 300 μm each, and the temperature field is shown at $z = 1.5$ mm and $f = 18$ Hz: a, $2d$ = 0.0 mm, amplitude; b, $2d$ = 0.6 mm, amplitude; c, phase of b; d, $2d$ = 1.8 mm, amplitude; e, phase of d.

ser sources modulated in phase and a single laser source at twice the irradiance. If the in-phase laser sources are separated by $2d = 1.8$ mm, then Figs. 6c and 6d show the interference patterns as two maxima of equal magnitude along the line joining the intersection points of the laser beams with the surface (line *OP* in Fig. 5). An increase in the modulation frequency (Fig. 6e) enhances the resolution and accentuates the thermal-wave field maxima, as expected. The amplitude maxima in Figs. 6c and 6e are located at positions different from those of the exciting optical apertures, a characteristic of the superposition nature of the interferometric thermal-wave field. This phenomenon is entirely analogous to the positions of constructive interference fringes in Young's well-known optical interferometric experiment. It should also be noticed that the maximum amplitudes of the constructive interference fields in Fig. 6 decrease with increased separation. This is expected, since, in the limit of large separations (compared with the thermal diffusion length), the interaction between the two thermal-wave fields will become negligible. The interference field will then appear as two independent lobes such as the one shown in Fig. 2a. This trend is corroborated by the phase interferograms of Figs. 6b, 6d, and 6f. Two phase-lag minima appear in the locations of the exciting laser beams in Figs. 6d and 6f at the same level; this is indicative of the essential decoupling of the two thermal-wave fields even at a separation distance of 1.8 mm, which is, however, large compared with the thermal diffusion length at 18 Hz in aluminum.

Figure 7 presents theoretical simulations of $|T^{(-)}(x, y, z)|$ and $\Psi^{(-)}(x, y, z)$ in a geometry completely analogous to that of Fig. 6 but for out-of-phase laser-beam modulation. In Fig. 7a the spatial superposition of the two laser beams ($2d = 0$) results in the complete annihilation of the two interfering thermal-wave fields in the limit of total destructive interference. Similarly, the phase shift is undefined everywhere, as is the case with a zero-field phase. Numerically this appears as a 0/0 operation. This observation was first made experimentally in a nonscanned (i.e., spatially stationary) mode by Lehto *et al.*,[10] using an out-of-phase alternating beam method in photothermal microscopic studies of plasma-sprayed tungsten carbide coatings on stainless-steel plates. As the two sources are separated out, a finite interference field appears with a minimum (zero value) halfway between the sources, Fig. 7b. The amplitude maxima are located beyond the actual positions of the two laser sources for the same superposition reasons as those discussed above for the constructive interference patterns of Figs. 6c and 6e. The thermal-wave field phase (Fig. 7c) shows a steep steplike structure halfway between the laser sources with a shift $\Delta\phi$ of $\sim 175°$, i.e., of the order of π. This is indicative of the domination of the phase field by the phase of each source in the immediate neighborhood of the source. Figure 7c is useful as a visual measure of the spatial extent of the influence of each laser source at locations where the other source starts making a contribution. Similar observations can be made about the field generated by using a larger beam separation (Figs. 7d and 7e). A comparison of the relative amplitudes of the destructively interfering fields (Figs. 7a, 7b, and 7d) reveals a monotonic increase with increased separation, unlike the constructive interference field amplitude trends of Figs. 6a and 6c (monotonic decrease with increased separation). This results from the decreasing effects of interference with increasing source separation. Increased separation tends to cancel the destructive interference between the two thermal waves and to restore the two amplitudes toward the values representing the amplitude from each source alone, i.e., decoupled from the field generated by the other, out-of-phase, source.

3. EXPERIMENT AND RESULTS

The details of the instrumentation and experimental scheme for thermal-wave diffraction detection have been presented elsewhere.[11] A black-box type of description of the apparatus is shown in Fig. 8. The exciting beams were supplied from a Hughes Aircraft He–Ne laser delivering ~10 mW of power at 632.8 nm. The detector element was a 28-μm-thick polyvinylidene fluoride (PVDF) pyroelectric film with an upper (grounded) electrode made of standard Pennwalt Al–Ni layers (200-Å Ni covered with 600-Å Al).[12] The lower surface of the PVDF film was not electroded and was in contact with a brass pin of 0.8-mm circular tip diameter. In this arrangement the tip was able to monitor local charge changes on the PVDF surface that resulted from the photopyroelectric (P^2E) effect.[11,13] Conventional pyroelectric detection of thermal waves used in a scanned, spatially integrated detection mode was reported by Luukkala[14] and by Petts and Wikramasinghe.[15] A cylindrical aluminum sample (diameter $D = 1$ cm, thickness $L = 1.5$ mm) was mounted upon the upper flat surface of the PVDF P^2E detector, and intimate contact was ensured. At the lowest modulation frequency ($f = 18$ Hz) of our experiments, the thermal diffusion length in aluminum was[5]

$$\mu_s(f = 18 \text{ Hz}) = [k_s(18 \text{ Hz})]^{-1} = 1.2 \text{ mm} \ll D \tag{33}$$

so that the sample could be adequately approximated by a

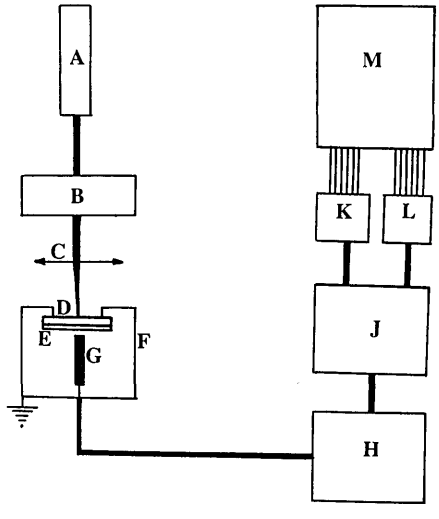

Fig. 8. Schematic diagram of apparatus used for photothermal-wave diffraction detection: A, He–Ne laser; B, mechanical chopper; C, lens; D, aluminum sample; E, PVDF film; F, metal shield; G, brass tip; H, preamplifier; J, lock-in analyzer; K, quadrature of signal to channel 1 of analog-to-digital converter; L, in-phase of signal to channel 0 of analog-to-digital converter; M, PDP/11 microcomputer.

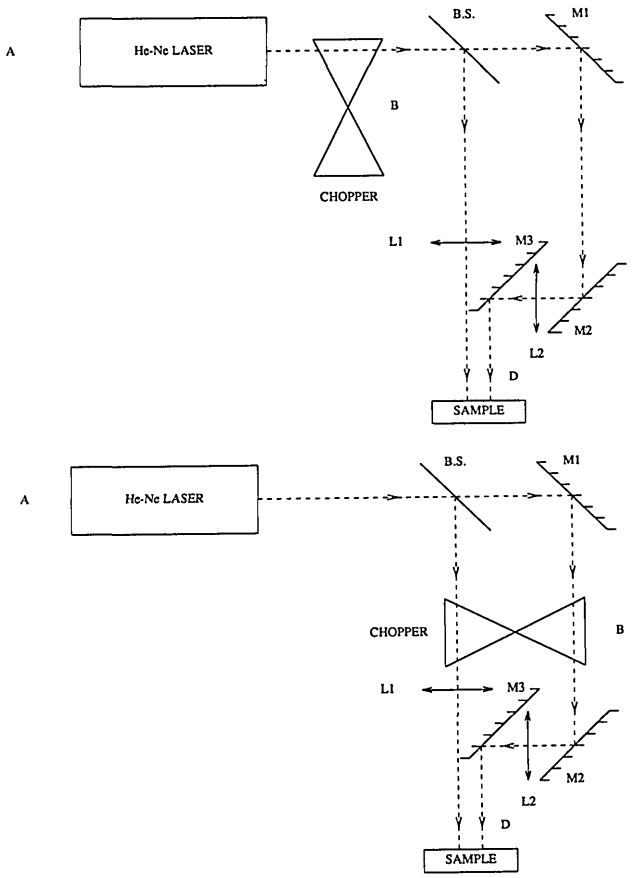

Fig. 9. Schematic diagrams of optical circuit used for photothermal-wave interference detection. Circuit replaces parts A–C of Fig. 8. B.S.'s, beam splitters; L's, lenses; M's, mirrors; D's, aluminum samples; B's, mechanical choppers; A, in-phase modulation; B, out-of-phase modulation.

radially semi-infinite aluminum solid. Furthermore, the condition $\mu_s(f)_{\max} < L$ ensured operation in the thermally thick regime, according to relation (11). In principle, the contributions to the signal from reflected (interfering) thermal waves at the back surface of the sample must be taken into consideration in interpreting the results.[3] This is also the essence of the thermal-wave interference effect described earlier by Bennett and Patty.[16] That effect is quite different in nature from the present interferometry; it refers to a one-dimensional depth interference manifested in the modulation-frequency dependence of the thermal-wave signal. That interference, albeit correctly defined for a spatially integrating detection geometry, cannot lead to the spatially resolved interference phenomena reported here. For backdetection (i.e., transmission-mode) thermal-wave techniques, heavily damped thermal-wave fields may be observed at thicknesses approximately five times the thermal diffusion length.[17] In the present geometry a contribution from twice-reflected thermal waves might be expected at $f =$ 18 Hz modulation, corresponding to one reflection at the sample's back surface followed by one more reflection at the front surface. The magnitude of such an added contribution to the thermal-wave field generated from the first transmission at the back would be decreased by a factor[18]

$$\sim\left(\frac{1-b}{1+b}\right)\exp(-2k_sL) \approx 0.97 \times \exp(-2.5) = 7.96 \times 10^{-2}, \tag{34}$$

where

$$b \equiv k_{\mathrm{PVDF}}\sqrt{\alpha_{\mathrm{Al}}}/k_{\mathrm{Al}}\sqrt{\alpha_{\mathrm{PVDF}}}$$

is an interfacial thermal-wave reflection coefficient, with[5] $k_{\mathrm{Al}} = 2.008 \times 10^2$ W/m K, $\alpha_{\mathrm{Al}} = 8.2 \times 10^{-5}$ m^2/sec, $k_{\mathrm{PVDF}} =$ 0.13 W/m K, $\alpha_{\mathrm{PVDF}} = 5.4 \times 10^{-8}$ m^2/sec.[12] From the good agreement between the theoretical results for semi-infinitely thick solids and the experimental results on finite-thick-

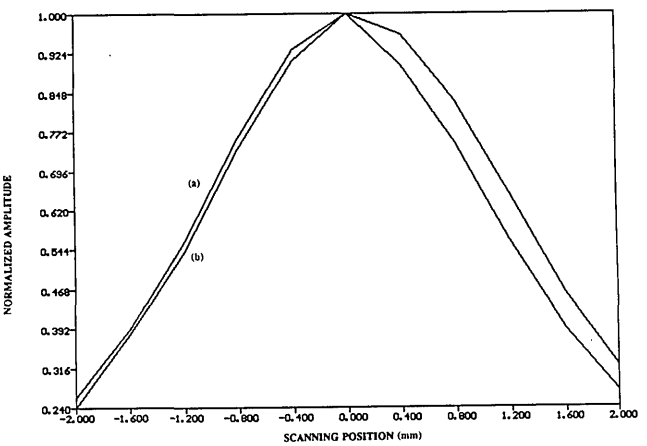

Fig. 10. Normalized experimental thermal-wave diffraction profiles along the (meridian) plane defined by the scanning laser beam and the probe pin. The patterns were generated with a beam waist/aperture of (a) 0.8 mm and (b) 0.03 mm. Modulation frequency $f =$ 20 Hz.

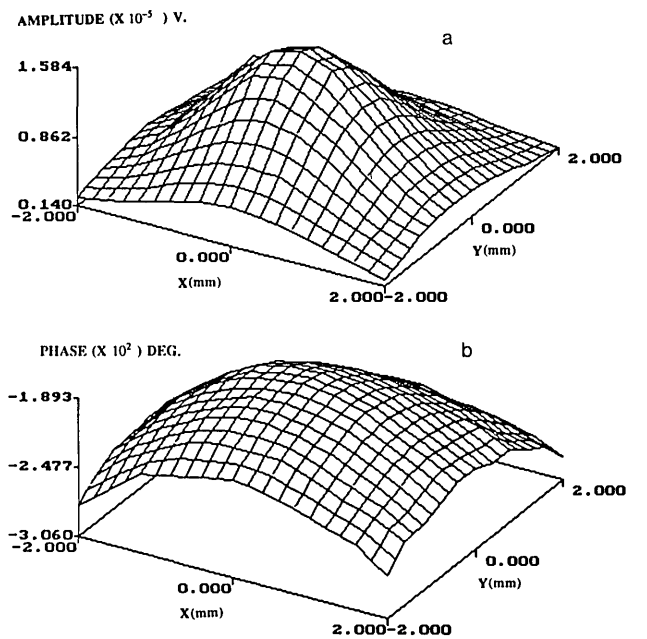

Fig. 11. Experimental diffraction patterns generated by a $w = 300$-μm laser beam and a 1.5-mm-thick aluminum sample. Modulation frequency 20 Hz: a, amplitude; b, phase. Compare with the theoretical prediction patterns of Fig. 2.

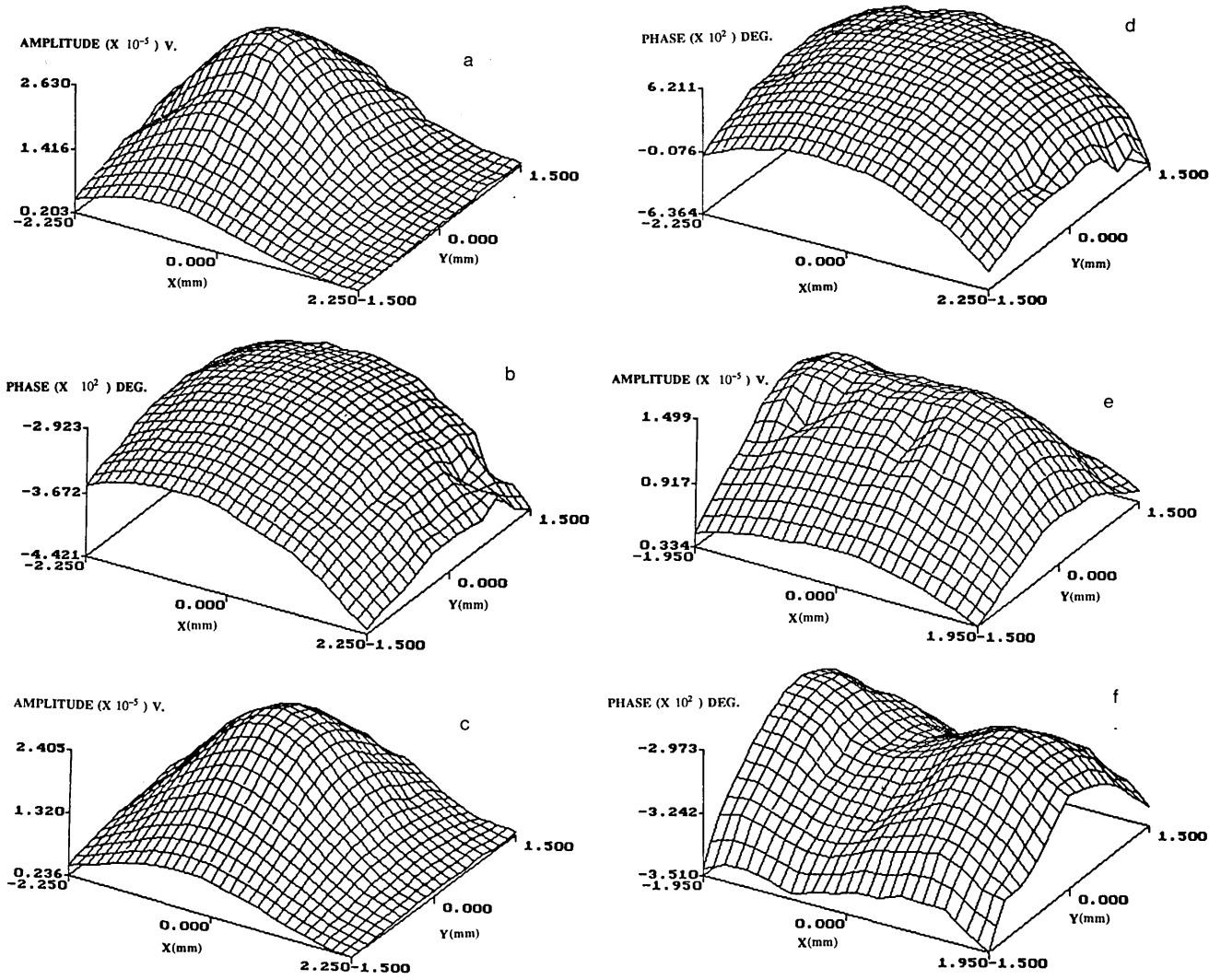

Fig. 12. Experimental constructive interference patterns generated by a geometry identical to that resulting in the theoretical patterns of Fig. 6. Modulation frequency 18 Hz; beam waists 300 μm; a, $2d$ = 0.6-mm amplitude; b, phase of a; c, $2d$ = 1.2-mm amplitude; d, phase of c; e, $2d$ = 2.4-mm-amplitude; f, phase of e. Compare with trends in Fig. 6.

ness aluminum shown below, it was concluded *a posteriori* that such a reflected thermal-wave contribution to our spatial diffraction and interference signals was essentially negligible and that the experimental scans could be adequately described by the semi-infinite thickness model of Section 2 above. The fact that the aluminum sample used in this study was much thicker than the PVDF detector ensured[19] that the transducer would operate as a thermometer, producing a pyroelectric charge proportional to the PVDF thickness-averaged local temperature in the pyroelectric element, which is essentially equal to the local temperature change at the sample–transducer interface. Therefore the P^2E signals thus obtained were found to be proportional to the local values of the thermal-wave field at the probe pin position over the plane of the sample's back surface.

Figure 9 shows modifications made to parts B and C of Fig. 8 for dual laser-beam incidence on sample D and in-phase (Fig. 9A) and out-of-phase (Fig. 9B) irradiance modulation. Figure 9A is a variant of an equivalent experimental method for local in-phase thermal-wave field sampling illustrated by Busse and Renk.[20] In their experiment a Golay detector was used to monitor local backsurface infrared radiation emission resulting from in-phase modulation of two laser beams heating the front surface of the sample. In the present experiments the metallic pin (Fig. 8) was used in lieu of the infrared sensor. In all cases a 10-mW He–Ne laser beam was used to excite thermal waves in the aluminum sample. The beam splitter of Fig. 9 was a variable-absorbance neutral-density filter, mounted upon a micrometer stage to produce two laser beams of approximately equal irradiance at the sample surface. The optical absorption coefficient of the aluminum sample surface was further increased by a thin film of black paint on the surface, which minimized reflections and yielded maximum photothermal signals. Scanning of the laser beam(s) was performed with the probe pin remaining stationary and in contact with the unelectroded PVDF film surface at the center of the exposed film area.

Figure 10 shows experimental diffraction profiles with the

aperture size (laser-beam waist) as a parameter. The sizes were chosen to be 0.03 and 0.8 mm to permit a direct comparison with the simulations of Fig. 4. General qualitative agreement of both sets of profiles is observed, with the experimental diffraction profile of the 0.8-mm aperture being slightly more broadened than that of the 0.03-mm aperture. This trend is in agreement with the theoretical prediction of little sensitivity to the aperture size in the range $w \ll R$, covering both aperture values in Figs. 4 and 10.

Figure 11 shows entire thermal-wave diffraction patterns (amplitude and phase) generated when a 0.3-mm laser-beam is scanned on the aluminum sample surface. The experimental parameters chosen were identical to those chosen for the theoretical simulations of Fig. 2, and thus a direct comparison is possible. The qualitative agreement (overall spatial distribution profiles–morphologies of amplitude and phase images) between Figs. 2 and 11 is excellent and shows that the semi-finite solid approximation assumed in the theoretical formulation[2] is essentially adequate for analyzing diffraction results from our 1.5-mm-thick sample.

Figure 12 shows experimental results of constructive interference patterns in the geometry of Figs. 5 and 9A. For this experiment the $2d$ = 0.0-mm and $2d$ = 0.6-mm interference fields were obtained by a slight tilt of mirror M_3 to render the two beams coincident or nearly so. No significant disturbance of the (measured) Gaussian profile of the beams results from this operation. The amplitude sequence in Figs. 12a, 12c, and 12e shows a monotonic maximum amplitude decrease with increasing separation, as predicted and discussed in conjunction with Fig. 6. Both amplitude and phase shapes display trends with increasing separation qualitatively similar to those of Fig. 6, with the individual source contributions to the thermal-wave interference pattern becoming resolvable at a minimum distance of 1.8 ± 0.2

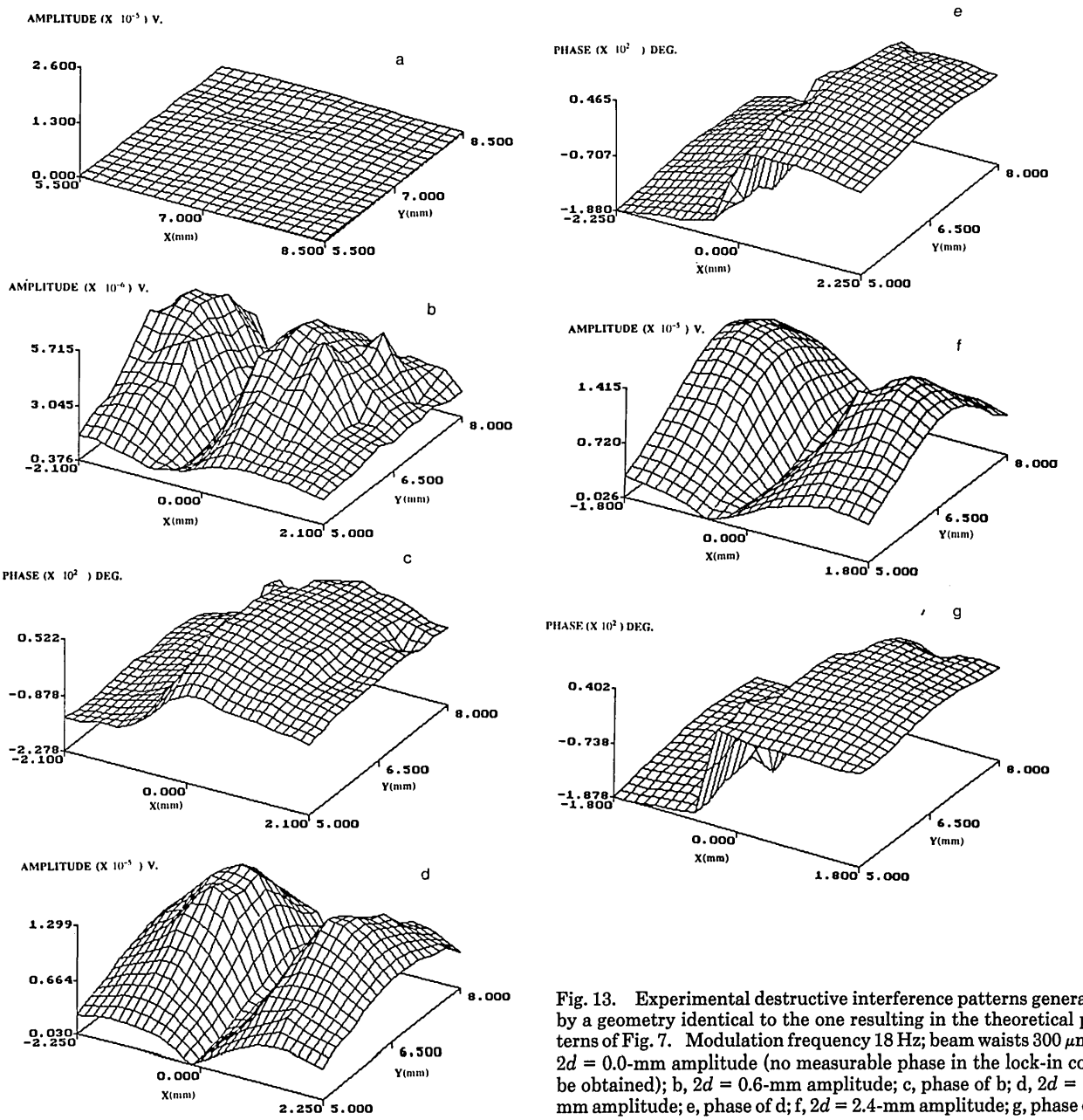

Fig. 13. Experimental destructive interference patterns generated by a geometry identical to the one resulting in the theoretical patterns of Fig. 7. Modulation frequency 18 Hz; beam waists 300 μm; a, $2d$ = 0.0-mm amplitude (no measurable phase in the lock-in could be obtained); b, $2d$ = 0.6-mm amplitude; c, phase of b; d, $2d$ = 1.8-mm amplitude; e, phase of d; f, $2d$ = 2.4-mm amplitude; g, phase of f.

mm. The interference pattern at zero laser-beam distance is of magnitude larger than that of Fig. 12a, as expected, and is similar to that of Figs. 2a and 2b. Therefore it is not shown in the sequence of Fig. 12.

Figure 13 is a sequence of experimental thermal-wave destructive interference patterns in the geometry of Figs. 5 and 9. The amplitude sequence (Figs. 13a, 13b, 13d, and 13f) shows clear evidence of complete field annihilation (destructive interference) with spatially overlapping sources (Fig. 13a), becoming less effective with increasing beam separation distance. This is in excellent qualitative agreement with the theoretical sequence of Fig. 7. The agreement extends to field maximum amplitude increases with increasing separation, a minimum halfway between the two beams, amplitude peaks somewhat beyond the actual laser-beam positions, and a steplike structure of the associated phases, Figs. 13c, 13e, 13g, of $\Delta\phi \approx \pi$.

4. QUANTITATIVE ASPECTS AND DISCUSSION

The good *qualitative agreement* between the theoretical simulations of Section 2 and the experimental results of Section 3 demonstrates that photothermal waves exhibit strong wavelike behavior both in diffraction through a generating small aperture and in interference when two coherent or anticoherent thermal-wave fields are brought within interaction distance. A closer look at the field profiles, however, reveals that there is little *quantitative agreement* between experiment and theory. The typical situation may be observed, in its simplest form, in the broadening of the experimental diffraction profiles of Fig. 10 compared with the (supposedly identical) theoretical ones of Fig. 4. Similar broadening effects may be seen in all experimental features of diffraction or interference and cannot be explained by our simple theoretical model.[2] The cause of this discrepancy has been sought in the finite size of the brass probe tip, which was used to collect all data. On the contrary, all theoretical simulations assumed an infinitesimal size probe, providing thermal-wave field values at particular coordinate points along the cross-sectional (x, y) observation plane (Fig. 1) in the sample. The diffraction field amplitude [Eq. (7)] was chosen as a suitable expression for study of the integrating effects of the probe pin size. In the case of our 1.5-mm-thick Al sample at $f = 18$-Hz modulation frequency and $w = 300$-μm optical aperture, the following simplifications occur:

$$\left.\frac{k_s(\omega)}{2R}\right|_{\max} = \frac{1}{2z}\left(\frac{\omega}{2\alpha_{\mathrm{Al}}}\right)^{1/2} \approx 28\ \mathrm{cm}^{-2} \tag{35}$$

and

$$1/w^2 = 1.1 \times 10^3\ \mathrm{cm}^{-2}, \tag{36}$$

so that

$$F_1(R, w) \approx w^{-2} \gg \frac{k_s(18\ \mathrm{Hz})}{2R} = F_2(R). \tag{37}$$

In view of relation (37), Eq. (7) may be simplified:

$$|T(r_0, z)| \approx \frac{k_s z w^2}{16\sqrt{2}R^2} \exp\left\{-k_s R\left[1 + \left(\frac{k_s w^2}{2R}\right)^2\left(\frac{r_0}{R}\right)^2\right]\right\}. \tag{38}$$

Now, since $k_s/2R|_{\max} \approx 28\ \mathrm{cm}^{-2}$, $w^2 \approx 9 \times 10^{-4}\ \mathrm{cm}^2$, and $r_0/R < 1$, we may write

$$\left(\frac{k_s w^2}{2R}\right)^2\left(\frac{r_0}{R}\right)^2 < 6.35 \times 10^{-4} \ll 1 \text{ (for aluminum)}. \tag{39}$$

Under these conditions, relation (38) may be written as

$$|T(r_0, z)| \approx C\frac{\exp(-k_s R)}{R^2}, \tag{40}$$

where C is a constant independent of R:

$$C \equiv \frac{k_s z w^2}{16\sqrt{2}}. \tag{41}$$

The geometry of a finite-sized tip of radius r_1 is shown in Fig. 14. The variable r indicates the position of a coordinate point on the surface of the pin detector, a distance r_1' from the pin symmetry axis $0'$. The average value of the thermal-wave field over the pin cross-sectional area is

$$\langle T(r_0, z; r_1)\rangle = \frac{1}{A}\int_0^{2\pi} d\theta \int_{r_0}^{r_{\max}} |T(r_0, z)| r dr, \tag{42}$$

where (Fig. 14)

$$r_{\max}(\theta) = (r_0^2 + r_1^2 - 2r_0 r_1 \cos\theta)^{1/2} \tag{43}$$

and

$$A = \int_0^{2\pi} d\theta \int_{r_0}^{r_{\max}} r dr = \pi r_1^2 \tag{44}$$

is the cross-sectional area of the pin. Use of Eq. (3) and relation (40), with a change of variables, and the constancy of z along the (x, y) plane yield

$$\langle T(r_0, z; r_1)\rangle = \frac{C}{A}\int_0^{2\pi} d\theta \int_R^{R_{\max}} \frac{\exp(-k_s R_0)}{R_0} dR_0, \tag{45}$$

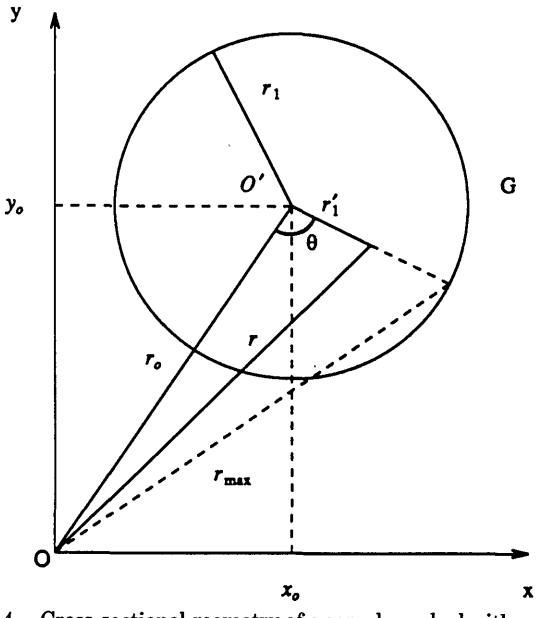

Fig. 14. Cross-sectional geometry of a sample probed with a cylindrical pin of radius r_1 positioned at distance r_0 from the origin. In the configuration of Fig. 8, the tip G is facing and is in contact with the unelectroded PVDF surface.

where

$$R_{\max}(\theta) \equiv (r_0^2 + r_1^2 + z^2 - 2r_1 r_0 \cos\theta)^{1/2}. \quad (46)$$

Equation (45) may be written in terms of the exponential integral function (Ref. 21, p. 228, entry 5.1.1)

$$\langle T(r_0, z; r_1)\rangle = \frac{C}{A}\left[\int_0^{2\pi} E_1(k_s R)\mathrm{d}\theta - \int_0^{2\pi} E_1[k_s R_{\max}(\theta)]\mathrm{d}\theta\right]. \quad (47)$$

For computational purposes the following series expansion may be used for small values of the argument (Ref. 21, p. 228, entry 5.1.11):

$$E_1(x) = -\gamma - \ln x - \sum_{n=1}^{\infty} \frac{(-1)^n x^n}{nn!}, \qquad |\arg(x)| < \pi,$$

$$\gamma = 0.5772156649 \text{ (Euler's constant)}. \quad (48)$$

Appendix B gives the details of the mathematical development based on Eq. (47), which leads to the analytical form for the pin-surface-averaged thermal-wave diffraction field amplitude [Eq. (B26)].

Computer calculations and comparisons of the expression for $\langle T(r_0, z; r_1)\rangle$ with the experimental data of curve (b) of Fig. 10 were performed by allowing the probe tip radius r_1 to

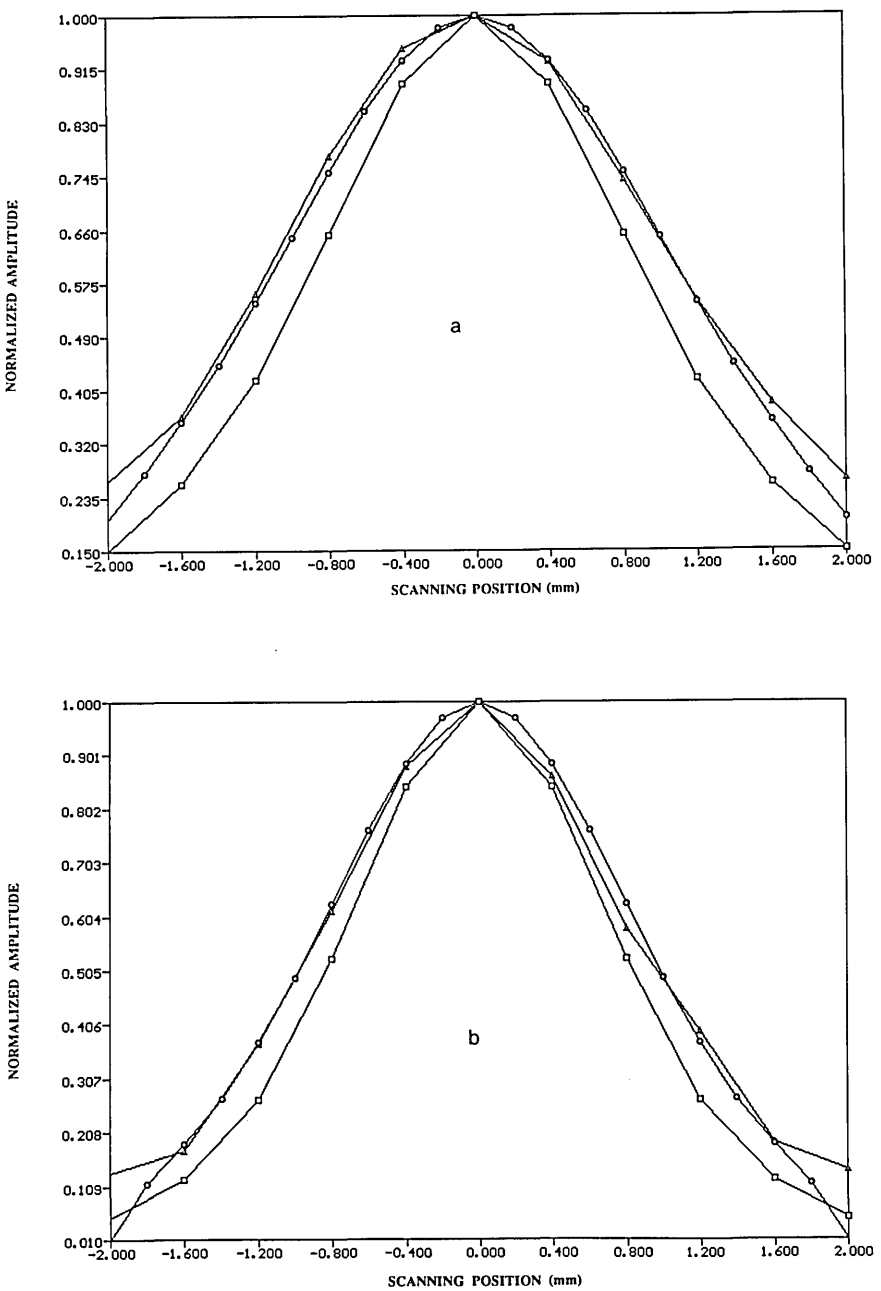

Fig. 15. a, Effect of finite-sized metal pin probe on the normalized thermal-wave diffraction profile of Fig. 10: triangles, experimental profile; circles, best fit of Eq. (B26) to the experimental profile using $\alpha_{Al} = 0.98$ cm^2/sec and $(r_1)_{eff} = 3.5$ mm; squares, normalized theoretical profile [expression (40)]. Modulation frequency: 20 Hz. b, Same as a but with $f = 100$ Hz.

vary in order to obtain the best fit. The results are shown in Fig. 15a for 20-Hz diffraction data. Also shown in Fig. 15a is the theoretical curve for $|T(r_0, z)|$ [relation (40)] normalized to unity at the maximum. It can be seen that the best fit to the 20-Hz data is obtained with an effective probe tip radius $(r_1)_{\text{eff}} = 3.5$ mm and aluminum thermal diffusivity[5] 0.82 cm^2/sec. Figure 15b shows the best fit of Eq. (B26) to the experimental diffraction profile at 100 Hz. Again, the value of α_{Al} was set to 0.82 cm^2/sec, and the fit yielded the same $(r_1)_{\text{eff}} = 3.5$ mm, an excellent degree of self-consistency with the value obtained from the fit to the 20-Hz data. In view of the fact that several aluminum thermal diffusivity values have been tabulated[22] at room temperature, showing considerable spread, fits of Eq. (B26) to the experimental curves were further performed, keeping r_1 at its actual geometrical value of 0.8 mm and varying α_{Al} by ±20% of its previously assumed value.[5] No good fit to the data was possible, indicating that realistic variations of α_{Al} could not explain the difference between experimental and theoretical [relation (40)] profiles. It thus appears that a theoretical fit to the data of our photothermally induced diffraction field in aluminum is possible, the finite size of the probe pin being the only parameter to which the experimental profile broadening in Figs. 10 and 15 appears to be sensitive enough to give good agreement between experimental and theoretical line shapes. At this time the large discrepancy between $(r_1)_{\text{actual}}$ and $(r_1)_{\text{eff}}$ is not well understood; however, it is tentatively attributed to the contributions of stray capacitive coupling of the (exposed) vertical pin walls to the P^{2}E signals in the form of extraneous electric field lines terminating on lateral regions of the unelectroded PVDF film surface. Such excess capacitive formation has been shown to increase the effective contact area between the PVDF detector and the contacting probe pin[11] both experimentally[7] and theoretically.[23] This mechanism would increase the effective pin size and is currently under further investigation for a quantitative explanation of the observed discrepancy.

5. CONCLUSIONS

In this paper qualitative and quantitative aspects of optically induced thermal-wave field diffraction and interference have been investigated. Good overall qualitative agreement was found between photopyroelectric experimental scans from a thermally thick homogeneous aluminum sample of finite thickness and previously developed photothermal diffraction and interference theory valid for semi-infinite solids. A mechanism for quantitative agreement was possible only when the finite size of the probing metal tip was properly taken into account as a spatial field-integrating filter. A remaining pin-size discrepancy with the theory is likely due to 3-D capacitive effects at the pin–PVDF film interface.

APPENDIX A: SERIES EXPANSION REPRESENTATIONS OF THE FUNCTION $W(Z) = \exp(Z^2)\text{erfc}(Z)$ IN THE COMPLEX DOMAIN

The complex variable Z may be written in the polar form

$$Z = |Z|e^{i\theta}. \tag{A1}$$

Further, the complementary error function of a complex argument may be defined in terms of real and imaginary parts:

$$\text{erfc}(Z) \equiv \text{Re}[\text{erfc}(Z)] + i\,\text{Im}[\text{erfc}(Z)]. \tag{A2}$$

In order to evaluate $W(Z)$ anywhere in the complex plane, it is convenient to consider four sectors because of convergence requirements for erfc(Z) (Ref. 24):

In the sectors $-\frac{1}{4}\pi \le \theta \le \frac{1}{4}\pi$ and $\frac{3}{4}\pi \le \theta \le \frac{5}{4}\pi$, the erfc$(Z)$ converges. Separating out real and imaginary parts of $W(Z)$ yields

$$\text{Re}[W(Z)] = \exp(|Z|^2\cos 2\theta)\{\cos(|Z|^2\sin 2\theta)\text{Re}[\text{erfc}(Z)] - \sin(|Z|^2\sin 2\theta)\text{Im}[\text{erfc}(Z)]\} \tag{A3}$$

and

$$\text{Im}[W(Z)] = \exp(|Z|^2\cos 2\theta)\{\sin(|Z|^2\sin 2\theta)\text{Re}[\text{erfc}(Z)] + \cos(|Z|^2\sin 2\theta)\text{Im}[\text{erfc}(Z)]\}, \tag{A4}$$

where the following representations may be used[24]:

$$\text{Re}[\text{erfc}(Z)] = \begin{cases} 1 - (2/\sqrt{\pi})\displaystyle\sum_{n=0}^{\infty}(-1)^n \frac{|Z|^{2n+1}\cos[(2n+1)\theta]}{n!(2n+1)} & \text{(Taylor)} \\ (2/\sqrt{\pi})\exp(-|Z|^2\cos 2\theta)\displaystyle\sum_{n=0}^{\infty}(-1)^n \frac{(2n-1)!!\cos[|Z|^2\sin 2\theta + (2n+1)\theta]}{2^{n+1}|Z|^{2n+1}} & \text{(asymptotic)} \end{cases}, \tag{A5}$$

$$\text{Im}[\text{erfc}(Z)] = \begin{cases} -(2/\sqrt{\pi})\displaystyle\sum_{n=0}^{\infty}(-1)^n \frac{|Z|^{2n+1}\sin[(2n+1)\theta]}{n!(2n+1)} & \text{(Taylor)} \\ -(2/\sqrt{\pi})\exp(-|Z|^2\cos 2\theta)\displaystyle\sum_{n=0}^{\infty}(-1)^n \frac{(2n-1)!!\sin[|Z|^2\sin 2\theta + (2n+1)\theta]}{2^{n+1}|Z|^{2n+1}} & \text{(asymptotic)} \end{cases}, \tag{A6}$$

where

$$-\tfrac{1}{4}\pi \le \theta \le \tfrac{1}{4}\pi, \qquad \tfrac{3}{4}\pi \le \theta \le \tfrac{5}{4}\pi.$$

In the sectors $\frac{1}{4}\pi \le \theta \le \frac{3}{4}\pi$ and $\frac{5}{4}\pi \le \theta \le \frac{7}{4}\pi$, the erfc$(Z)$ diverges. In these sectors, however, the function $W(Z)$ itself converges, so that the following expressions may be used:

$$\text{Re}[W(Z)] = \text{Re}[\exp(Z^2)\text{erfc}(Z)] \tag{A7}$$

and

$$\text{Im}[W(Z)] = \text{Im}[\exp(Z^2)\text{erfc}(Z)], \tag{A8}$$

where[24]

$$\mathrm{Re}[\exp(Z^2)\mathrm{erfc}\,Z] = \begin{cases} \exp(|Z|^2\cos 2\theta)\cos(|Z|^2\sin 2\theta) - (2/\sqrt{\pi})\displaystyle\sum_{n=0}^{\infty}\frac{2^n|Z|^{2n+1}\cos[(2n+1)\theta]}{(2n+1)!!} & \text{(Taylor)} \\ (1/\sqrt{\pi})\displaystyle\sum_{n=0}^{\infty}(-1)^n\frac{(2n-1)!!\cos[(2n+1)\theta]}{2^n|Z|^{2n+1}} & \text{(asymptotic)} \end{cases}, \quad \text{(A9)}$$

$$\mathrm{Im}[\exp(Z^2)\mathrm{erfc}\,Z] = \begin{cases} \exp(|Z|^2\cos 2\theta)\sin(|Z|^2\sin 2\theta) - (2/\sqrt{\pi})\displaystyle\sum_{n=0}^{\infty}\frac{2^n|Z|^{2n+1}\sin[(2n+1)\theta]}{(2n+1)!!} & \text{(Taylor)} \\ -(1/\sqrt{\pi})\displaystyle\sum_{n=0}^{\infty}(-1)^n\frac{(2n-1)!!\sin[(2n+1)\theta]}{2^n|Z|^{2n+1}} & \text{(asymptotic)} \end{cases}, \quad \text{(A10)}$$

where

$$\tfrac{1}{4}\pi \le \theta \le \tfrac{3}{4}\pi, \qquad \tfrac{5}{4}\pi \le \theta \le \tfrac{7}{4}\pi.$$

Computationally, the point $|Z| = 3.9$ was found[24] to be a good transition point from the Taylor to the asymptotic expansion, even though the exact value varies slightly for different θ's throughout the complex plane.

APPENDIX B: SERIES EXPANSION REPRESENTATION OF THE PIN-SURFACE-AVERAGED THERMAL-WAVE DIFFRACTION FIELD AMPLITUDE

The photothermal Gaussian aperture function

$$T_0(\zeta) = \exp(-\zeta^2/w^2) \quad \text{(B1)}$$

has been shown to lead to the (approximate) diffraction thermal-wave field of relation (40), which is valid for an aluminum semi-infinite sample excited with a $w = 0.3$-mm laser beam at $f = 18$ Hz:

$$|T(r_0, z)| \approx C\frac{\exp(-k_sR)}{R^2}, \quad \text{(B2)}$$

so that the average field sensed by a cylindrical metal pin detector is given by Eq. (47):

$$\langle T(r_0, z; r_1)\rangle = \frac{C}{A}[I_1(r_0, z) - I_2(r_0, z; r_1)], \quad \text{(B3)}$$

where we have defined

$$I_1(r_0, z) \equiv \int_0^{2\pi} E_1(k_sR)\mathrm{d}\theta = 2\pi E_1(k_sR) \quad \text{(B4)}$$

and

$$I_2(r_0, z; r_1) \equiv \int_0^{2\pi} E_1[k_sR_{\max}(\theta)]\mathrm{d}\theta = 2\int_0^{\pi} E_1(k_s\sqrt{r_0^2 + r_1^2 + z^2 - 2r_1r_0\cos\theta})\mathrm{d}\theta. \quad \text{(B5)}$$

The integral $I_2(r_0, z; r_1)$ may be transformed by using the definition of the exponential integral function

$$E_1[k_sR_{\max}(\theta)] = \int_{k_sR_{\max}(\theta)}^{\infty}\frac{e^{-y}}{y}\mathrm{d}y \quad \text{(B6)}$$

so that, on setting $y = k_sR_{\max}(\theta)x$, we obtain

$$I_2(r_0, z; r_1) = \int_1^{\infty}\frac{\mathrm{d}x}{x}Q(x), \quad \text{(B7)}$$

where

$$Q(x) \equiv 2\int_0^{\pi}\exp[-k_sxR_{\max}(\theta)]\mathrm{d}\theta. \quad \text{(B8)}$$

From the definition of $R_{\max}(\theta)$ [Eq. (46)], it can be shown that

$$\mathrm{d}\theta = \frac{1}{r_0r_1}\frac{R_{\max}\mathrm{d}R_{\max}}{\sin\theta}. \quad \text{(B9)}$$

With further manipulation of Eqs. (B8) and (B9) we find that

$$Q(x) = 4\int_0^a\frac{e^{-x\zeta}\zeta\mathrm{d}\zeta}{[(a^2 - \zeta^2)(\zeta^2 - b^2)]^{1/2}}, \quad \text{(B10)}$$

where

$$a \equiv k_s[(r_0 + r_1)^2 + z^2]^{1/2} \quad \text{(B11a)}$$

and

$$b \equiv k_s[(r_0 - r_1)^2 + z^2]^{1/2}. \quad \text{(B11b)}$$

Now let $\zeta = a\sin q$; Eq. (B10) becomes

$$Q(x) = 4\int_{q_0}^{\pi/2}\frac{\exp(-xa\sin q)\sin q\mathrm{d}q}{(\sin^2 q - \sin^2 q_0)^{1/2}}, \quad \text{(B12)}$$

where

$$q_0 \equiv \sin^{-1}(b/a). \quad \text{(B13)}$$

Equations (B7) and (B12) yield

$$I_2(r_0, z; r_1) = 4\int_{q_0}^{\pi/2}\frac{\sin q\mathrm{d}q}{(\sin^2 q - \sin^2 q_0)}\int_1^{\infty}\frac{\exp(-xa\sin q)}{x}\mathrm{d}x, \quad \text{(B14)}$$

so that a variable change to $y = xa\sin q$ finally gives the form

$$I_2(r_0, z; r_1) = 4\int_{q_0}^{\pi/2}\frac{E_1(a\sin q)\sin q\mathrm{d}q}{(\sin^2 q - \sin^2 q_0)}. \quad \text{(B15)}$$

Expanding the function $E_1(a\sin q)$ according to Eq. (48) for small values of the argument gives the series representation

$$I_2(r_0, z; r_1) = -4\left[\frac{\pi}{2}\gamma + \frac{\pi}{2} ln\left(\frac{a+b}{2}\right) + \sum_{n=1}^{\infty} \frac{(-1)^n a^n}{nn!} J_n(b/a)\right], \quad \text{(B16)}$$

where we have defined

$$J_n(b/a) \equiv \int_{q_0}^{\pi/2} \frac{\sin^{n+1} q\,dq}{(\sin^2 q - \sin^2 q_0)^{1/2}}. \quad \text{(B17)}$$

In order to obtain explicit expressions for the integrals $J_n(b/a)$, the following relationship (a simplified version of Ref. 25, p. 169, entry 2.585) may be utilized:

$$\int \frac{\sin^{n+1} x}{\Delta}\,dx = \frac{1}{nk^2}\left[\Delta \sin^{n-2} x \cos x + (n-1)(1+k^2) \times \int \frac{\sin^{n-1} x}{\Delta}\,dx - (n-2)\int \frac{\sin^{n-3} x}{\Delta}\,dx\right], \quad n \geq 3, \quad \text{(B18)}$$

where

$$\Delta \equiv (1 - k^2 \sin^2 x)^{1/2}. \quad \text{(B19)}$$

Equation (B17) may also be written in the form

$$J_n(b/a) = \frac{a}{b}\int_{q_0}^{\pi/2} \frac{\sin^{n+1} q\,dq}{[(a/b)^2 \sin^2 q - 1]^{1/2}}. \quad \text{(B20)}$$

For Eq. (B18) to be applicable to the integral in Eq. (B20), a modification must be made according to a transformation given by Gradshteyn and Ryzhik in Ref. 25, p. 175: $\Delta \rightarrow i\sqrt{-\Delta^2}$. Substitution into Eq. (B18) gives the desired relation:

$$\int \frac{\sin^{n+1} q\,dq}{(k^2 \sin^2 q - 1)^{1/2}} = \frac{1}{nk^2}\left[-(k^2 \sin^2 q - 1)^{1/2} \sin^{n-2} q \cos q + (n-1)(1+k^2)\int \frac{\sin^{n-1} q\,dq}{(k^2 \sin^2 q - 1)^{1/2}} - (n-2) \times \int \frac{\sin^{n-3} q\,dq}{(k^2 \sin^2 q - 1)^{1/2}}\right], \quad n \geq 3. \quad \text{(B21)}$$

Equations (B20) and (B21) may now provide a useful recursion formula for J_n:

$$J_n(b/a) = \frac{1}{n}\{(n-1)[1 + (b/a)^2]J_{n-2}(b/a) - (n-2)(b/a)^2 J_{n-4}(b/a)\}, \quad n \geq 5. \quad \text{(B22)}$$

The first few J_n integrals may be evaluated directly by using results found in Ref. 25, Sec. 2.548, pp. 162–175:

$$J_1(b/a) = \mathbf{E}\{[1 - (b/a)^2]^{1/2}\}, \quad \text{(B23a)}$$

$$J_2(b/a) = \frac{\pi}{4}[1 + (b/a)^2], \quad \text{(B23b)}$$

$$J_3(b/a) = \tfrac{1}{3}(2[1 + (b/a)^2]\mathbf{E}\{[1 - (b/a)^2]^{1/2}\} - (b/a)^2 \mathbf{K}\{[1 - (b/a)^2]^{1/2}\}), \quad \text{(B23c)}$$

and

$$J_4(b/a) = \frac{\pi}{4}\left\{\frac{3}{4}[1 + (b/a)^2]^2 - (b/a)^2\right\}, \quad \text{(B23d)}$$

where the functions $\mathbf{E}$ and $\mathbf{K}$ are complete elliptic integrals given in series representations by Ref. 25, p. 905, entries 8.113.1 and 8.114.1:

$$\mathbf{E}(x) \equiv \frac{\pi}{2}\left\{1 - \sum_{m=1}^{\infty}\left[\frac{(2m-1)!!}{2^m m!}\right]^2 \frac{x^{2m}}{2m-1}\right\} \quad \text{(B24)}$$

and

$$\mathbf{K}(x) \equiv \frac{\pi}{2}\left\{1 + \sum_{m=1}^{\infty}\left[\frac{(2m-1)!!}{2^m m!}\right]^2 x^{2m}\right\}. \quad \text{(B25)}$$

All higher J_n functions may be evaluated explicitly by using Eqs. (B23) and the recursion relation in Eq. (B22). Collecting terms, Eqs. (B3), (B4), (B16), (B22), and (B23) give the following analytical expression for the thermal-wave diffraction field amplitude averaged over the detection pin size:

$$\langle T(r_0, z; r_1)\rangle = \frac{2C}{r_1^2}\left(\ln\left(\frac{a+b}{2k_s R}\right) + k_s R - \frac{2a}{\pi}\mathbf{E}\{[1 - (b/a)^2]^{1/2}\} - \frac{1}{4}(k_s R)^2 + \frac{a^2}{8}[1 + (b/a)^2] - \sum_{n=3}^{\infty}\frac{(-1)^n}{nn!}\left[(k_s R)^n - \frac{2}{\pi}a^n J_n(b/a)\right]\right). \quad \text{(B26)}$$

ACKNOWLEDGMENTS

The support of the Ontario Laser and Lightwave Research Center and of the Natural Sciences and Engineering Research Council of Canada is gratefully acknowledged. We also thank M. Mieszkowski and K. Ghandi for providing IBM PC graphics support for producing scanned field imaging patterns throughout this study.

REFERENCES

1. H. S. Carslaw and J. C. Jaeger, *Conduction of Heat in Solids*, 2nd ed. (Clarendon, Oxford, 1959), Chap. 2.6.
2. A. Mandelis, "Theory of photothermal-wave diffraction and interference in condensed media," J. Opt. Soc. Am. A **6**, 298–308 (1989).
3. M. Vaez Iravani and H. K. Wickramasinghe, "Scattering matrix approach to thermal wave propagation in layered structures," J. Appl. Phys. **58**, 122–131 (1985).
4. M. Vaez Iravani and M. Nikoonahad, "Photothermal waves in anisotropic media," J. Appl. Phys. **62**, 4065–4071 (1987).
5. A. Rosencwaig, *Photoacoustics and Photoacoustic Spectroscopy* (Wiley, New York, 1980), p. 96.
6. A. Rosencwaig and A. Gersho, "Theory of the photoacoustic effect with solids," J. Appl. Phys. **47**, 64–69 (1976).
7. A. Rosencwaig, "Photoacoustic microscopy," Am. Lab. **11**, 39–49 (1979).
8. M. Mieszkowski and A. Mandelis, "Photoelectric spatially resolved imaging of thermal wave fields," J. Opt. Soc. Am. A **7**, 552–557 (1990).
9. A. Mandelis, Y. C. Teng, and B. S. H. Royce, "Phase measurements in the frequency domain photoacoustic spectroscopy of solids," J. Appl. Phys. **50**, 7138–7148 (1979).
10. A. Lehto, M. Jokinen, J. Jaarinen, T. Tiusanen, and M. Luukkala, "Alternating beam method (ABM) in photothermal microscopy (PTM) and photoacoustic microscopy (PAM)," Electron. Lett. **17**, 540–541 (1981).

11. M. Mieszkowski, K. L. Leung, and A. Mandelis, "Photopyroelectric thermal wave detection via contactless capacitive polyvinylidene fluoride (PVDF)-metal probe-tip coupling," Rev. Sci. Instrum. **60,** 306–316 (1989).
12. KYNAR Piezo Film Technical Manual (Pennwalt Corporation, King of Prussia, Pa., 1983).
13. H. Coufal and A. Mandelis, "Photopyroelectric spectroscopy of semiconductors," in *Photoacoustic and Thermal Wave Phenomena in Semiconductors*, A. Mandelis, ed. (North-Holland, New York, 1987), Chap. 7, pp. 149–173.
14. M. Luukkala, "Photoacoustic microscopy at low modulation frequencies," in *Scanned Image Microscopy*, E. A. Ash, ed. (Academic, London, 1980), p. 273.
15. C. R. Petts and H. K. Wikramasinghe, "Photothermal spectroscopy on a microscopy scale," in *Proceedings of the IEEE Ultrasonics Symposium* (Institute of Electrical and Electronics Engineers, New York, 1981), pp. 832–836.
16. C. A. Bennett and R. R. Patty, "Thermal wave interferometry: a potential application of the photoacoustic effect," Appl. Opt. **21,** 49–54 (1982).
17. G. Busse, "Imaging with optically generated thermal waves," IEEE Trans. Sonics Ultrason. **SU-32,** 355–364 (1985).
18. A. Mandelis and M. M. Zver, "Theory of photopyroelectric spectroscopy of solids," J. Appl. Phys. **57,** 4421–4430 (1985).
19. H. J. Coufal, R. K. Grygier, D. E. Horne, and J. E. Fromm, "Pyroelectric calorimeter for photothermal studies of thin films and adsorbates," J. Vac. Sci. Technol. A **5,** 2875–2889 (1987).
20. G. Busse and K. F. Renk, "Stereoscopic depth analysis by thermal wave transmission for nondestructive evaluation," Appl. Phys. Lett. **42,** 366–368 (1983).
21. M. Abramowitz and A. Stegun, *Handbook of Mathematical Functions*, 9th ed. (National Bureau of Standards, Washington, D.C., 1970).
22. Y. S. Touloukian, R. W. Powell, C. Y. Ho, and M. C. Nicolaou, *Thermal Diffusivity* (IFI/Plenum, New York, 1973).
23. A. Mandelis, "A variational-Green's function approach to theoretical treatment and applications of the capacitance of three-dimensional geometries," Can. J. Phys. **60,** 179–195 (1981).
24. A. Mandelis and B. S. H. Royce, "Nonradiative lifetime measurements in time-domain photoacoustic spectroscopy of condensed phases," J. Appl. Phys. **51,** 610–615 (1980).
25. I. S. Gradshteyn and I. M. Ryzhik, *Table of Integrals, Series, and Products* (Academic, New York, 1980).